

Pressure loss and heat transfer characterisation of intersecting hole heat exchangers

Imran Naved*, David Gillespie

The University of Oxford, Department of Engineering Science, Oxford Thermofluids Institute, The Southwell Building, Oxford OX2 0ES, United Kingdom

ARTICLE INFO

Keywords:

Intersecting film cooling passages
Loss coefficient
Convective heat transfer
HTC
Experimental

ABSTRACT

Intersecting cooling holes allow very high density heat exchangers to be implemented in the cooling systems of gas turbine blades. The pressure loss and heat transfer characteristics caused by the highly turbulent flow at intersections are poorly understood. These are characterised experimentally and numerically for a single intersection of two equal diameter holes at 90° or 60°/120° angles of intersection, 0%, 10%, 49% and 88% offset. Large variations in pressure loss occur for a given intersection geometry; dependent on the mass flow splits, and the level of offset. Pressure losses range from 4 to more than 30 inlet dynamic heads. This allows the flow distribution in an engine application to be tuned, allowing for manufacturing uncertainties. Heat transfer coefficient (HTC) distributions measured in single intersections are reported. These show clear enhancement associated with stripping the fluid boundary layer and mixing of the bulk flow. High local heat transfer gradients were observed at the intersections and circumferentially averaged Nusselt number enhancement of up to 5 found where the degree of pipe intersection is significant. The HTC distributions allow the required packing of hole intersections while controlling the pressure margin. The experimental data are replicated in CFD studies which show good agreement within experimental uncertainty. Thus more detailed numerical models can be relied on for a full range of intersection angles and offsets. Extending the modelling to include multiple linked intersections confirmed that data measured in single intersections are applicable to a matrix of multiply intersecting holes.

1. Introduction

Turbine vanes and blades have long been considered one of the most difficult cooling challenges with heat loads of several kW/cm² being typical in the hottest engine parts. While the gas turbine blade may be considered a heat exchanger, it is unusual in that its aim is to maintain its wall temperature at a prescribed maximum level. For a modern single crystal super nickel alloy blade the metal temperature limit is about 1450 K, lying between the high pressure coolant (850–950 K) and the mainstream gas temperature (≈2000 K). Unlike a process heat exchanger the coolant stream can be ejected through the blade into the mainstream to provide an enthalpy absorbing layer next to the metal surface. The momentum of the mainstream flow is used to turn the exiting coolant onto the blade surface, but at the leading edge the flow is stagnant and the ejected flow tends to separate from the surface. This poses particular problems; a solution which maximises the internal cooling, minimises the metal volume and lowers the exit velocity of the flow is desirable. A cooling scheme using a matrix of intersecting holes has the potential to fulfil these requirements.

A typical nozzle guide vane is shown in Fig. 1 along with a schematic of the flow through the interesting hole cooling scheme proposed in this paper and a conventional leading edge hole arrangement. Provided the pressure loss at the intersections is known a near contiguous film can be ejected at very low velocity onto the external surface using the proposed solution. Previous work [1,2] have principally considered a planar implementation of such schemes, where passages fully intersect. Nowlin et al. [3] conducted studies of partially intersecting cooling matrices for blade leading edges. Later [4] developed a better understanding of the pressure loss and heat transfer coefficient (HTC) for a small number of intersection geometries.

The present study extends this work for a single pipe intersection over the full range of possible flow distributions in each inlet/outlet combination at feasible angles of intersection and offset between holes. For a subset of the cases, HTC distributions were experimentally determined using the transient thermochromic liquid crystal (TLC) technique [5]. The experimental campaign is complemented by a thorough computational fluid dynamics (CFD) study of both the pressure drop and heat transfer across the intersections. The experimental

* Corresponding author.

E-mail address: imran.naved@eng.ox.ac.uk (I. Naved).

<https://doi.org/10.1016/j.ijthermalsci.2020.106313>

Received 26 June 2019; Received in revised form 3 February 2020; Accepted 6 February 2020

Available online 10 March 2020

1290-0729/© 2020 The Authors.

Published by Elsevier Masson SAS. This is an open access article under the CC BY-NC-ND license

(<http://creativecommons.org/licenses/by-nc-nd/4.0/>).

Nomenclature

A_{pipe}	Pipe cross-sectional area, m^2
c_p	Specific heat capacity at constant pressure, $\text{J kg}^{-1} \text{K}^{-1}$
C_d	Discharge coefficient
d_{pipe}	Pipe diameter, m
d_{orifice}	Orifice diameter, m
h	Heat transfer coefficient, $\text{W m}^{-2} \text{K}^{-1}$
K	Loss coefficient
k	Thermal conductivity, $\text{W m}^{-1} \text{K}^{-1}$
L	Pipe length from inlet, m
M	Mach number
\dot{m}	Mass flow rate, kg s^{-1}
Nu	Nusselt number, $\frac{hd}{k}$
p	Pressure, Pa
q	Heat flux, W m^{-2}
Q	Volumetric flow rate, $\text{m}^3 \text{s}^{-1}$
Re	Reynolds number, $\frac{\rho u d}{\mu}$
T	Temperature, K
t	Time, s
u	Velocity, m s^{-1}
z	Pipe offset, m
β	Eq. (7) thermal response coefficient
γ	Ratio of specific heats
θ	Angle subtended between two intersecting pipes, deg
μ	Dynamic viscosity, Pa s
ρ	Density, kg m^{-3}

Subscripts

atm	Atmospheric
g	Gas
h	Wall friction
i	Initial
s	Surface
w	Wall
x	Intersection
o	Total
i,j,1,2,3,4	Generic and particular pipe identifiers

and numerical HTC distributions are compared for various intersection geometries, showing good agreement. Finally, the analysis is extended for multiple intersections, proving that the results applicable for a single intersection can be applied for a matrix.

1.1. Flow through intersecting holes

In a cooling network constructed from a matrix of intersecting passages, the flow direction and pressure losses are determined from the inlet and exit boundary conditions to the system, and each individual flow intersection. At a single intersection, four key flow scenarios are possible, though some are unlikely because of the general pressure gradient from the inner to outer side of the turbine blade or vane. The four flow scenarios possible at an intersection are shown diagrammatically in Fig. 2. Intersections with fewer than four branches or sharp turns may be modelled by nulling the flow in appropriate branches at a network node. Transiently the flow scenarios may vary at a particular intersection — for example at low frequency if there is a sharp change in operating condition, or high frequency because of wake passing events in the engine.

For a single intersection of two holes with nominally equal diameter, two main geometry variables need to be considered: namely the angle of intersection (θ) and the offset of the holes one from another (z) (Fig. 4). The angle θ is defined to be 0° when the pipes are parallel. The offset z is defined as the distance between pipe centrelines and is expressed as a percentage of the total diameter of the pipe, thus a full intersection is a $\frac{z}{d} = 0\%$ offset case. If pipe 1 is defined such that it always carries the largest inlet volumetric flow rate, Q_1 , then all possible flows in the system can be fully described by the two non-dimensional flow parameters $\frac{Q_3}{Q_1}$ and $\frac{Q_2}{Q_1}$. Thus, the four flow scenarios can be mapped onto a $\frac{Q_3}{Q_1}$ vs. $\frac{Q_2}{Q_1}$ space as shown in Fig. 3. Note that Q_4 follows by continuity and that the regions labelled A', B', C', D' are mirror images of the four flow scenarios indicated in Fig. 2.

1.2. Loss coefficients and the additive loss model

In a flow network solver, loss coefficients (K) are typically used to scale pressure losses with the dynamic head in the flow. Gerhart et al. [6] related the loss in total pressure to the incoming dynamic head as:

$$K = \frac{p_{o,\text{inlet}} - p_{o,\text{exit}}}{\frac{1}{2} \rho u^2} \quad (1)$$

Where there is variable flow between inlet and outlet, the change in static head in the system is scaled by an inlet dynamic head and the outlet flow specified. For cooling passages where loss generating features are widely separated, an additive loss model is appropriate. The overall loss K associated with a particular node of a network of flow branches is then described by:

$$K = K_h + K_x, \quad (2)$$

where K_h and K_x are losses due to pipe friction and the branch or intersection respectively. K_h can be determined on the basis of the internal roughness of cooling passages and so it is only necessary to determine K_x through appropriate experimental, numerical or analytical modelling. In this paper a decision has been made to use the maximum inlet dynamic head as the denominator in Eq. (1). i.e. $\frac{1}{2} \rho \left(\frac{Q_1}{A_{\text{pipe}}} \right)^2$.

Note that care must be taken in comparing results with other workers as Zhang et al. [2] and Nowlin et al. [4] use the average velocity in all inlet pipes to generate the dynamic head. In generating lookup tables of loss coefficients, Q_1 is the highest inlet flow rate. The three loss coefficients required to define the full system are chosen as the pressure drop (or rise) from this inlet (1) to each of the other pipes (2, 3 & 4) — whether inlet or outlet. The loss coefficients are then sensibly denoted by K_{12} , K_{13} and K_{14} respectively.

For consistency with previous results by Nowlin et al. [4], the loss coefficients are henceforth defined by considering the normalised drop in static pressure across an intersection. Whilst this is true for equal inlet and outlet flows; this would not scale correctly for the full range of flow splits and the dynamic component can be accounted for as follows:

$$K_{o,12} = K_{12} + 1 - \left(\frac{Q_2}{Q_1} \right)^2 \quad (3)$$

$$K_{o,13} = K_{13} + 1 - \left(\frac{Q_3}{Q_1} \right)^2 \quad (4)$$

$$K_{o,14} = K_{14} + 1 - \left(1 + \frac{Q_2}{Q_1} - \frac{Q_3}{Q_1} \right)^2 \quad (5)$$

As mixing losses have historically been notoriously difficult to capture accurately using numerical tools, an experimental approach was first used to measure the pressure loss coefficients at appropriate, engine representative conditions as described below. Subsequent numerical studies were then used to interrogate the flow field to determine the loss mechanisms in the holes.

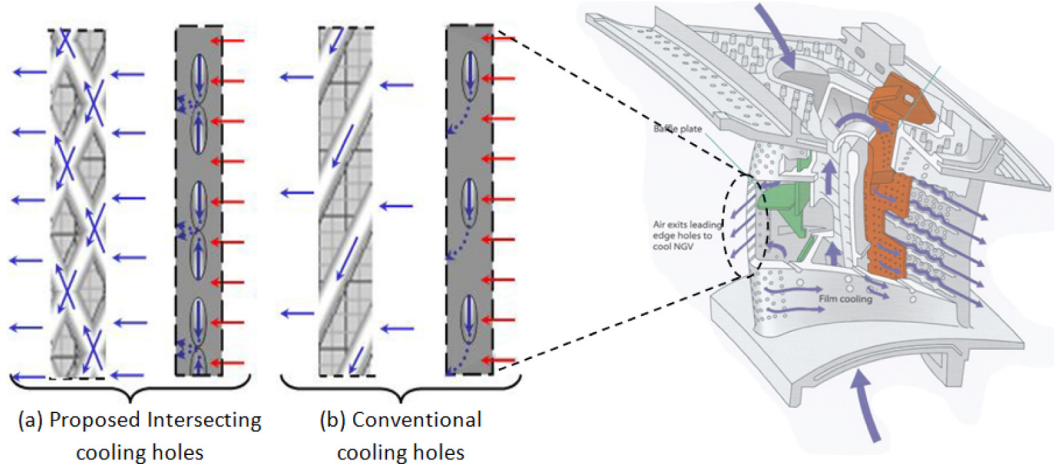


Fig. 1. (a) Proposed intersecting passage layout and (b) a representative intersecting passage layout for a representative nozzle guide vane cooling scheme (after [3] and [7]). The internal passage arrangement and breakout to the external surface are illustrated.

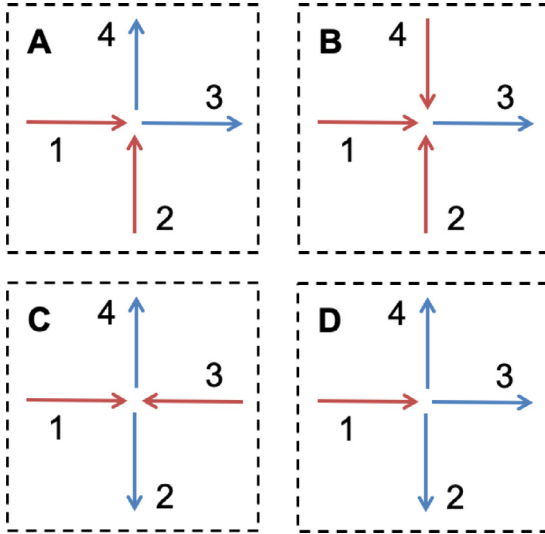


Fig. 2. Possible flow scenarios for a four pipe intersection. (flow may be zero in any of the pipes 2–4).

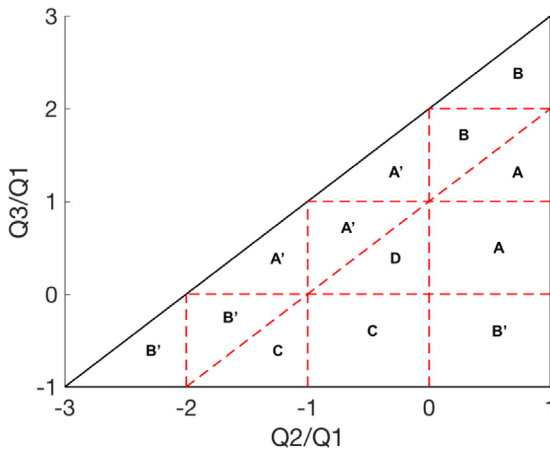


Fig. 3. 2D flow map, showing the mapping of flow scenarios for the case that Q_1 is always the largest inlet flow. (The sign convention for the flow in each branch is that shown in Fig. 2.)

2. Experimental design

A large scale experimental rig was designed through simple dimensional scaling. The non-dimensional parameters governing the system behaviour may be written as:

$$\phi(K_{1j} = \frac{p_1 - p_j}{\frac{1}{2} \rho (\frac{Q_1}{A_{\text{pipe}}})^2}, \frac{Q_j}{Q_1}, Re = \frac{\rho u d}{\mu}, \frac{z}{d}, \theta,$$

$$M = \frac{u_1}{\sqrt{\gamma R T_g}}, \frac{T_w}{T_g}, Nu = \frac{h d}{k} \Big|_{j=2-4} = 0. \quad (6)$$

In this paper turbine blade internal cooling features are considered for installation near the leading edge of a high pressure turbine blade where the pressure margin is low. For isentropic expansion over a range of pressure margins ($\frac{p_{0,\text{coolant}}}{p_{s,\text{mainstream}}} = 0 - 6.5\%$) across the whole engine, the flow Mach number remains below $M = 0.3$ and need not be matched provided the flow also remains incompressible in the experiment. The effect of the ratio $\frac{T_w}{T_g}$ is low in a passage where the heat capacity of the flow is high compared to the heat flux from the wall, and its effect on reported Nusselt number can be analytically scaled [8]. $\frac{T_w}{T_g}$ may principally effect the flow through the energisation of the thermal boundary layer, and by changing the rate of temperature drop in the coolant fluid. Thus to measure loss coefficients and local Nusselt number distributions, once the correctly scaled geometry is chosen, appropriate Reynolds number and flow rate ratios between the incoming pipes are set. It should be noted that the flow loss is dominated by fluid mixing events at the intersection and thus the loss coefficients have been measured in an isothermal environment. The effect of heat transfer on the system losses could be further investigated numerically but is beyond the scope of this paper. As the flow is considered fully turbulent in most cooling scenarios, moderate Reynolds numbers ranging 0–60,000 in each leg of the test rig were chosen for loss measurements; the lowest non-zero Reynolds being 5000. Engine representative Reynolds numbers were chosen such that they are similar to those expected in turbine blades or vanes ($Re = 2.0 - 6.5 \times 10^4$).

Cold flow tests were conducted to measure the loss coefficient. As the transient liquid crystal technique (TLC) was to be used for heat transfer measurements, the model scale was chosen such that the maximum expected heat flux would remain lower than 20 kW m^{-2} , resulting in pipes of uniform diameter 15.4 mm. Typical cooling passages in turbine blades feature diameters of the order of 0.6 mm, resulting in passages around 25 times engine scale. A set of interchangeable

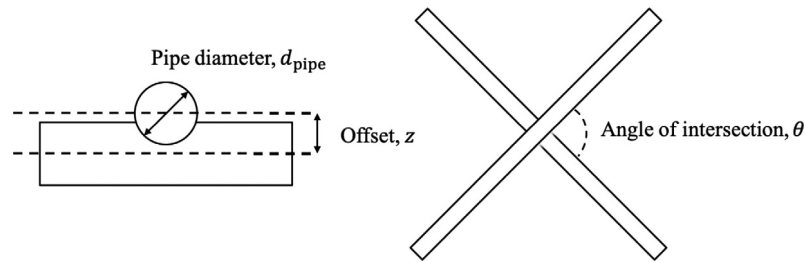


Fig. 4. Geometry variables for two intersecting passages.

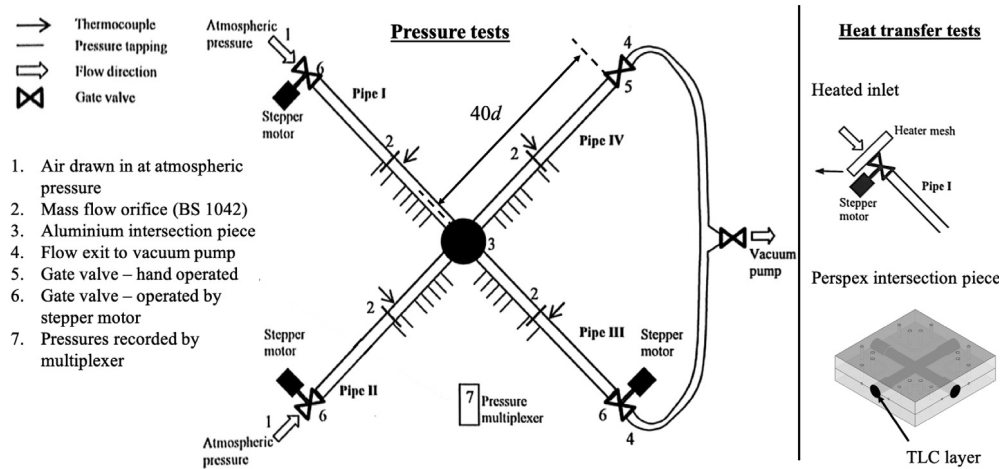


Fig. 5. Schematic of the single intersection test rig. For heat transfer tests the aluminium test piece is replaced by Perspex and a heater is installed at the entrance to one of the pipes feeding the intersection.

intersections were milled into solid aluminium or Perspex test pieces into which each feed or exit pipe was connected. At the intersection the holes are offset circumferentially by $\theta = 60^\circ$ or 90° and axially by a $\frac{z}{d} = 0\%, 10\%, 49\%$ and 88% . Care is taken to ensure no disturbance of the boundary layer at the junction between the incoming pipes and the flow manifold. At each inlet and outlet, gate valves driven by stepper motors are used to adjust the total flow and flow splits allowing data collection to be automated for a given intersection geometry.

The experimental test rig used to measure the loss coefficient for flow through a single intersection is shown schematically in Fig. 5. Air at atmospheric conditions is drawn through the inlet pipe gate valve(s) by a suction pump far downstream of the test section. Flow enters each pipe through a $20d$ length upstream of a BS 1042 mass flow orifice metre [9], and is delivered to the intersection along a further $20d$ development length. At the pipe section in closest proximity to the intersection, five 1 mm diameter static pressure tappings are used to measure the wall friction-driven pressure drop approaching the intersection. Flows exit the intersection through pipes configured identically to the inlets, finally passing into flexible tubing $40d$ downstream from the intersection and onwards to a vacuum pump. The pipes are drawn aluminium tubing with as manufactured hydraulically smooth inner surface finish, EN 0.0014 mm.

To determine the loss coefficient, the total mass flow rate and the flow split between the pipes is set and the static pressure distribution in each pipe determined. To eliminate bias errors a multiplexer and single pressure transducer are used for all static pressure tapping readings, each of which are averaged from 100 samples. From these data, the frictional pressure drop in each pipe is determined and extrapolated linearly to the centre of the intersection. The pressures at this location are then used to populate the pressure differences in the loss coefficients derived in Eq. (6) as shown in Figs. 6 and 7. For each intersection geometry an automated process is used to collect data at 39 equally distributed data points such that extrapolation to the outer edges is not

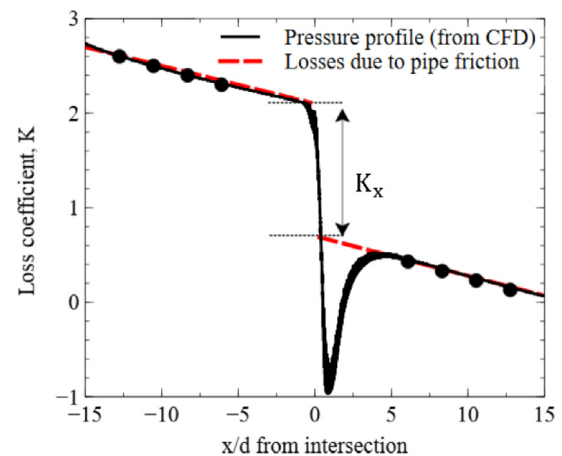


Fig. 6. The local pressure drop in the vicinity of the intersection as modelled using CFD.

necessary. The automated control system allowed required flow rates and flow distributions to be achieved within 2% of the specified values.

For heat transfer tests, an engine representative gas to wall temperature difference is not required, and the flow through one of the inlets is heated using a fast response mesh heater to raise its temperature by about 70°C in a near step change. For the heat transfer tests the intersections are manufactured from Perspex, a transparent insulator, which is coated with a $30\ \mu\text{m}$ thick layer of thermochromic liquid crystals which selectively reflect visible light with peak intensity at 30°C , 35°C and 40°C . Calibration of all the liquid crystals was performed in-situ: the change in liquid crystal colour adjacent to a surface thermocouple is recorded as the surface temperature is increased over

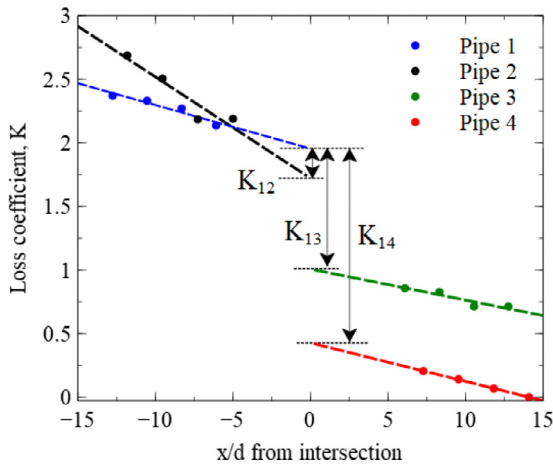


Fig. 7. Sample experimental data with equal flows of $Re = 30,000$ in each pipe.

a fine series of steady-state temperatures covering the full colour range of the liquid crystals. In-situ calibration removes the distortion effects caused by lighting or the local white balance of the cameras.

The gas temperature rise, measured with a fast response K-type thermocouple is modelled as a series of ramps of slope m_i and a 1D transient heat transfer model is used to determine the local heat transfer coefficient distributions at each pixel location on the surface:

$$T_w = T_0 + \sum_{i=1}^n m_i t \left(1 - \frac{2}{\beta_i \sqrt{\pi}} + \frac{1 - \exp(\beta_i^2) \operatorname{erfc}(\beta_i)}{\beta_i^2} \right),$$

$$\beta_i = \frac{h(t - t_i)^{1/2}}{\sqrt{\rho c_p k}}, \quad m_i = \frac{(\Delta T_{g,\infty})_i}{\Delta t}. \quad (7)$$

Full details of the process used to calculate the HTC distribution for the intersection are described in [10]. The heat transfer coefficients are driven by flow from all of the inlet flows, and to account for this are based on the local adiabatic wall temperature from which an effectiveness of each inlet flow can be determined. This allows the heat transfer coefficients to be scaled to engine operating conditions.

2.1. Uncertainty analysis

Using a typical set of experimental results ($Re_1 = 30,000$, $Re_2 = 10,000$, $Re_3 = 30,000$, $Re_4 = 10,000$) the uncertainty in mass flow rate and the calculated pressure loss coefficients are determined using Moffat's error propagation method [11] defined as:

$$\delta X = \sqrt{\sum_{i=1}^N \left(\frac{\partial X}{\partial Y_i} \delta Y_i \right)^2}, \quad (8)$$

where each variable is given as $X = X(Y_1, Y_2, \dots, Y_N)$. Here, X is the variable which is calculated from the measurements, Y_i , using data from the experiment. The uncertainties in Y_i , denoted by δY_i , are determined by the uncertainties of each measurand.

As shown in Table 1, the expected error in each measurand is reported and the total root-sum square (RSS) error in Reynolds number and mass flow rate (\dot{m}) is 3.34 and 2.17% respectively. It is notable here that the pressure at each tapping is measured using a single pressure transducer which eliminates bias offset errors, but the gain and precision error of the pressure transducer calibration needs to be included. These are available from the manufacturer data sheet and measured data. The full scale output for the transducers is 72 mbar and an arbitrary error in the pressure measurements of 20 Pa is considered for each transducer. For this typical case the RSS error in loss coefficient was shown to lie between 15.9 and 24.9% dependent on the flow split and level. The lack of noise seen in the output data used to generate

Table 1

Error contributions and overall uncertainty in Reynolds number, mass flow rate and loss coefficient.

Parameter	Baseline value	Uncertainty (value)	Uncertainty (%)
Measured parameters			
d_{orifice} (mm)	11	0.05	2.38%
d_{pipe} (mm)	15.4	0.25	5.82%
P_{atm} (mbar)	1013.25	1.3	<0.01%
T_{atm} (K)	293	1	0.01%
$P_{\text{static,upstream}}$ (mbar)	893.25	2	<0.01%
C_d	0.62	0.02	1.0%
$\Delta P_{\text{transducer}}$ (mbar)	72	2	2.50%
Derived parameters			
Re	37 504	1253	3.34%
\dot{m} (kg s ⁻¹)	0.00824	0.00018	2.17%
K_{12}	0.46	0.115	24.94%
K_{13}	0.52	0.116	22.39%
K_{14}	0.77	0.123	15.95%

Table 2

Error contributions and uncertainty for the highest HTC level (397.5 W/mK).

Parameter	Baseline value	Uncertainty (value)	Uncertainty (%)
Measured parameters			
t (s)	30	0.04	0.07%
$\sqrt{\rho c k}$ (J m ⁻² K ⁻¹ s ^{-0.5})	569	29	5.37%
T_g (K)	343	0.3	3.68%
T_i (K)	293	1	5.73%
$\Delta T_{\text{crystal}}$ (K)	35	0.1	8.12%
HTC discretisation (levels)	100	0.5	0.5%
Derived parameters			
HTC (W m ⁻² K ⁻¹)	397.5	50	12.55%
Effectiveness	0.65	0.0076	1.16%

the pressure loss maps suggests, however, that this is an overestimate of the overall error observed.

As described in [12], in transient narrow band liquid crystal experiments, the uncertainty in the experimental determination of HTC can be broken down into three different components: uncertainty in the experimental measurements that feed into the calculation of HTC; the uncertainty in matching the theoretical intensity history with the experimental history and the uncertainty due to the assumption of a semi-infinite plate. It is assumed that the error of the latter two components are small.

The error due to measurements is shown in Table 2. The components are taken to be independent although this is not necessarily the case, as for example, errors in the initial and gas temperatures will be common mode (and somewhat negating) with the liquid crystal calibration. A pixel by pixel uncertainty can be determined for the transient narrow band liquid crystal experiments yielding a total RSS error of 12.55% in HTC and 1.16% in effectiveness (adiabatic wall temperature).

3. Numerical CFD study

The experimental test conditions along with additional intersection geometries were modelled using ANSYS Fluent 17.2. The modelling improved confidence in the experimental results and allowed better insight to be gained into the flow physics at the hole intersections.

The intersections were modelled with identical intersection angles and offset as in the experimental configurations. ANSYS ICEM CFD 17.2 was employed to generate unstructured meshes using an octree mesh method with a very small global element seed size of 0.001 m. The volume mesh consisted of a tetra/mixed mesh and an additional 12 prism layer mesh was employed at the passage walls to better model the boundary layer region. The growth factor from the wall to the passage centreline is 1.2 to minimise potential numerical discontinuities.

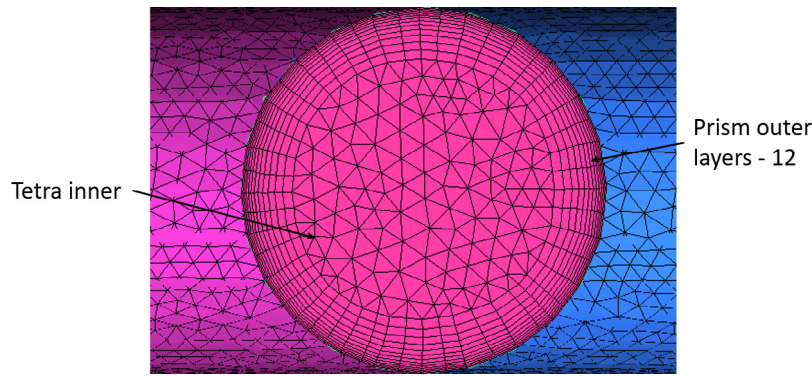


Fig. 8. Hybrid grid inlet quarter-plane mesh.

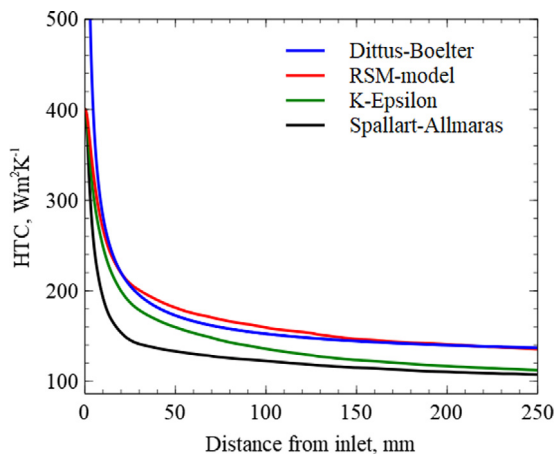


Fig. 9. Comparison of turbulence models.

Particular meshing difficulties were encountered where the offset is slight and vanishingly small volumes are generated. Nonetheless the resulting meshes had average $y^+ = 1$ in the surface boundary elements, suggesting that the laminar sub-layer close to the wall is adequately modelled for heat transfer purposes. A cross-section through a typical mesh is shown in Fig. 8. It should be noted that the extent of the CFD model is limited to a domain $20d$ upstream and downstream of the intersection. A uniform inlet velocity condition has been applied at these inlets so that fully developed flow does not hold upstream of the intersections, as was the case in the experimental work.

As the flow conditions are incompressible, several possible means of defining boundary conditions are acceptable. Here a velocity inlet with changing mass flow split between exit flows was employed and thus Reynolds numbers were matched to the experimental test conditions.

The Reynolds Stress (RSM) turbulence was used with RANS CFD. Fig. 9 shows the circumferentially averaged HTC distribution for an equal mass split simulation (90° , $z/d = 0$, $Re_1 = Re_2 = Re_3 = Re_4 = 30,000$) case with heated walls using a number of available turbulence models. The results upstream of the intersection are compared to the Dittus–Boelter correlation for turbulent pipe flow with inlet correction applied, where the RSM model captures the HTC most accurately.

The local HTC in CFD was calculated from two simulations run at two different wall temperatures (350 and 300 K), such that the local gradient of q_w vs. T_w is then used to determine the HTC. This is equivalent to a value of HTC based on the local adiabatic wall temperature and is required as the driving gas temperature is dependent on the local mixing of the incoming gas streams.

Grid independence is conducted for this model by considering three mesh sizes with global element seed sizes of 0.001 m, 0.002 m and

0.0005 m (resulting in 1.3, 0.3 and 28 million cells respectively). It was found that an element seed size of 0.001 m gave HTC values within 1% of the higher density mesh.

4. Results and discussion

4.1. Pressure drop and loss coefficients

The key data reported in this paper are the distributions of the loss coefficient K_{12} , K_{13} and K_{14} . The 39 data points recorded can be plotted onto the 2D flow map as per Fig. 10. Thereafter, loss coefficient maps are generated by interpolating the data points within the full range of the flow map.

Loss coefficient maps for a 90° intersection with $\frac{z}{d} = 0\%$, 49% and 88% offsets are shown in Fig. 11.

Consider first the loss coefficient K_{12} for no offset ($\frac{z}{d} = 0\%$). In flow scenarios A and B (refer to Figs. 2 and 3 for the definition of the different flow scenarios) pipes 1 and 2 are both inlets to the system, and thus there is essentially no mechanism for mixing losses to propagate between the two cases. Furthermore, in flow scenario D, the inlet from pipe 1 is split between three exit pipes, with no additional loss caused by mixing with another incoming flow. Thus the region of maximum loss is associated with flow scenario C where the flow from pipe 1 exits into pipe 2 having met flow from pipe 3 which directly opposes this inlet flow. The level of the loss is maximum along the $\frac{Q_3}{Q_1} = -1$ line as the relative magnitude of the incoming flow is maximised here inducing strong mixing. Where the exit flow in pipe 2 is lower than either of the inlet flows, the loss is limited, but as the flow increases to be equal or higher than any of the incoming flows the mixing losses increase strongly and up to 4 inlet dynamic heads are lost in the intersection. This might be expected as the loss coefficient is based on the dynamic head of pipe 1, and so by simply increasing $\frac{Q_2}{Q_1}$, we might expect K_{12} also to increase. However K_{12} is maximised when the flow split between the exit pipes (1 & 4) in scenario C is in the ratio 3:1, as this asymmetric exit flow increases mixing losses. With no offset, the loss K_{12} is minimised in a band where the inflow Q_1 matches the outflow Q_3 , $\frac{Q_3}{Q_1} = 1$. However, note that this does not imply contiguous flow in this region.

When the offset is increases from $\frac{z}{d} = 0\%$ to $\frac{z}{d} = 49\%$ & 88%, there is a very marked increase in the level of K_{12} , although its distribution remains largely unchanged. Between $\frac{z}{d} = 0\%$ –49% the peak loss rises to 150% of the original value, but a further increase in offset causes a runaway increase in the maximum loss by a factor of approximately 6. This is perhaps unsurprising as the head loss in the flow must now be dominated by the small hole which connects the throughflow pipes. Here a secondary peak occurs at $\frac{Q_2}{Q_1} = -0.5$, indicating that although an asymmetric split in the exit flow still maximises the loss, it must do so by changing the nature of the mixing as flow passes through the

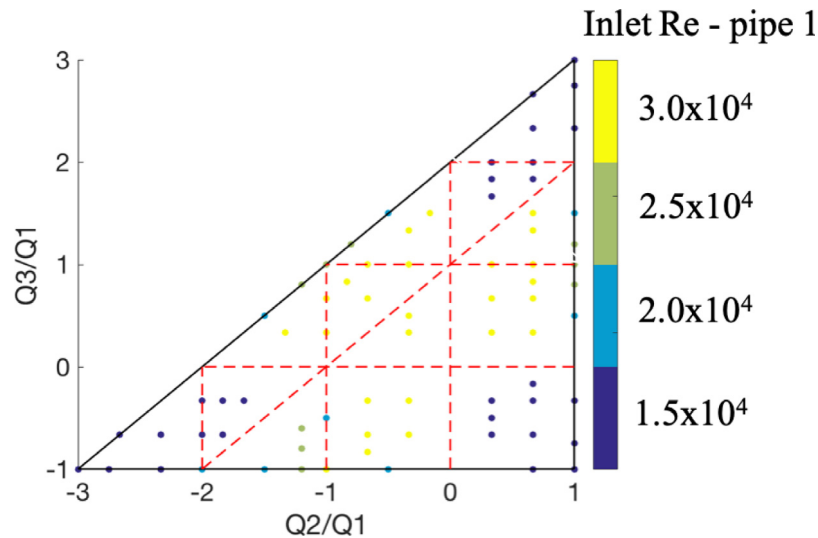


Fig. 10. Measured experimental data points with corresponding inlet Reynolds numbers.

intersection hole, and thus where the flow exits becomes irrelevant to the pressure seen in either of the exit passages.

K_{13} represents the loss between the pipe in which there is maximum incoming flow and the geometrically opposite pipe. In flow scenario A, flow from pipe 1 tends to flow into pipe 4, except in the limiting case where Q_2 and Q_4 tend to zero, in which case loss will be minimised. Thus K_{13} is low for this flow scenario. Likewise in flow scenario C, pipes 1 and 3 are both inlets and there pressures are inlet boundary conditions in the system. In flow scenario D the incoming flow in pipe 1 diffuses through the intersection into pipe 3, and unsurprisingly the loss is low, remembering that it is based on the incoming dynamic head in pipe 1. This leaves flow scenario B. In this case the incoming flow in pipe 1 is heavily mixed with two further incoming flows before exiting the system. This leads to the most severe mixing loss for the case of $\frac{z}{d} = 0$ with losses of up to 8 dynamic heads in this region: the overall range of the mixing loss is more than twice that of K_{12} . Again, the impact initial offsetting the geometry is to introduce additional loss, however the level of this additional loss is not as high for loss coefficient K_{13} as the pipes 1 and 3 are co-planar, and so while subject to additional mixing, the effect of jetting through the restricted area hole connecting the two pipes is reduced. Overall the maximum loss increases a maximum of about 14 inlet dynamic heads (see Fig. 11).

K_{14} is similar in nature to K_{12} and is maximised for flow scenarios A and C. In region C the behaviour is a precise mirror image of K_{12} with the loss maximises when the flow split between pipes 2 and 4 is 1:3 rather than 3:1. Exactly the same physical arguments as to the nature of the flow field pertain here. For the flow scenario A where flow is incoming in pipes 1 and 2, the loss K_{14} is higher than for K_{12} , as there is flow mixing between the inlet and exit flows with associated loss in pressure. Here the loss is maximised again for cases where the ratio of the flows in the outlet pipes 4 and 3 is in the ratio of approximately 3:1. This reflects enhanced mixing under these conditions, and the higher dynamic head in the outlet pipe. When the level of offset is increased, the loss in region C also increases, and at a rate that is very similar to that seen for K_{12} , but the loss in region A is almost uniform and in fact appears to reduce with increasing offset. This is perhaps unsurprising as there are two inlets in the case of flow scenario A, and these are separated when an offset is introduced, thus the flow exiting through pipe 4 will now preferentially be fed from pipe 2 rather than pipe 1 and there is likely to be less loss associated with this through-flow arrangement.

The data compares well with other workers' more limited results [2, 4]. A full range of offsets (0%, 10%, 49% and 88%) at the 90° orientation with equal mass splits ($Re_1 = Re_2 = Re_3 = Re_4 = 20,000$) show

reasonable agreement with values of K_{13} lying consistently within 0.5 of the data in the literature.

Fig. 12 shows further loss coefficient distributions for a 60° angle of intersection. (i.e. the included angle between branches 1 and 2 is 60°.) The losses are very similar in form to the 90° result plotted above. Notably, however, there are very slight increases in the level of loss coefficient for K_{12} and K_{14} and a more pronounced increase in K_{13} at $\frac{z}{d} = 0$. The effect of increasing offset on K_{12} plotted in the bottom line of the figure is slight until the offset reaches the highest tested value of 88%, where a maximum loss of 25 inlet dynamic heads is observed.

4.2. Numerical simulations

To validate the numerical simulations, the losses generated for the 90° intersection angle with 0% offset case are compared. Fig. 13 shows the difference in loss coefficient (ΔK) found using CFD compared to the experimental results for all 39 data points recorded. Over 80% of the CFD results match the experimental loss coefficients within ± 0.5 and over 97% of the CFD simulations match within ± 1 . This confirms that CFD can be used accurately to predict the loss coefficients across a single intersection and that this analysis can be extended for a greater range of intersection angles and offsets computationally.

4.3. Sensitivity analysis

An intersecting hole heat exchanger design, by its very nature can be susceptible to manufacturing errors. Errors in included angle are unlikely but offset between holes compared to a coplanar design is inevitable for drilled or EDM manufacture. The change in loss coefficient is compared to the coplanar case with increasing offset for three data points within scenario A (the most likely to be employed), in Figs. 14–16.

In Fig. 14, the mass flow rate is equal in all inlets and outlets, but in Figs. 15 and 16, the inlet flow ratio is 3:1 in inlets 1 and 2, and the outlet flows are in the same ratio with the highest flow rate being in outlet 3 for Fig. 15 and outlet 4 for Fig. 16. These latter cases are extreme flow splits that for most embodiments of a heat exchanger matrix would be unlikely to occur. Given the full range of loss coefficients observed, the system may be considered to show relatively low sensitivity to changing offset in the range $\frac{z}{d} = 0 - 49\%$. The precise loss mechanism changes however with the extent of the offset. For Fig. 14, with no offset the flow from inlets 1 and 2 are segregated and pass almost entirely separately to outlets 4 and

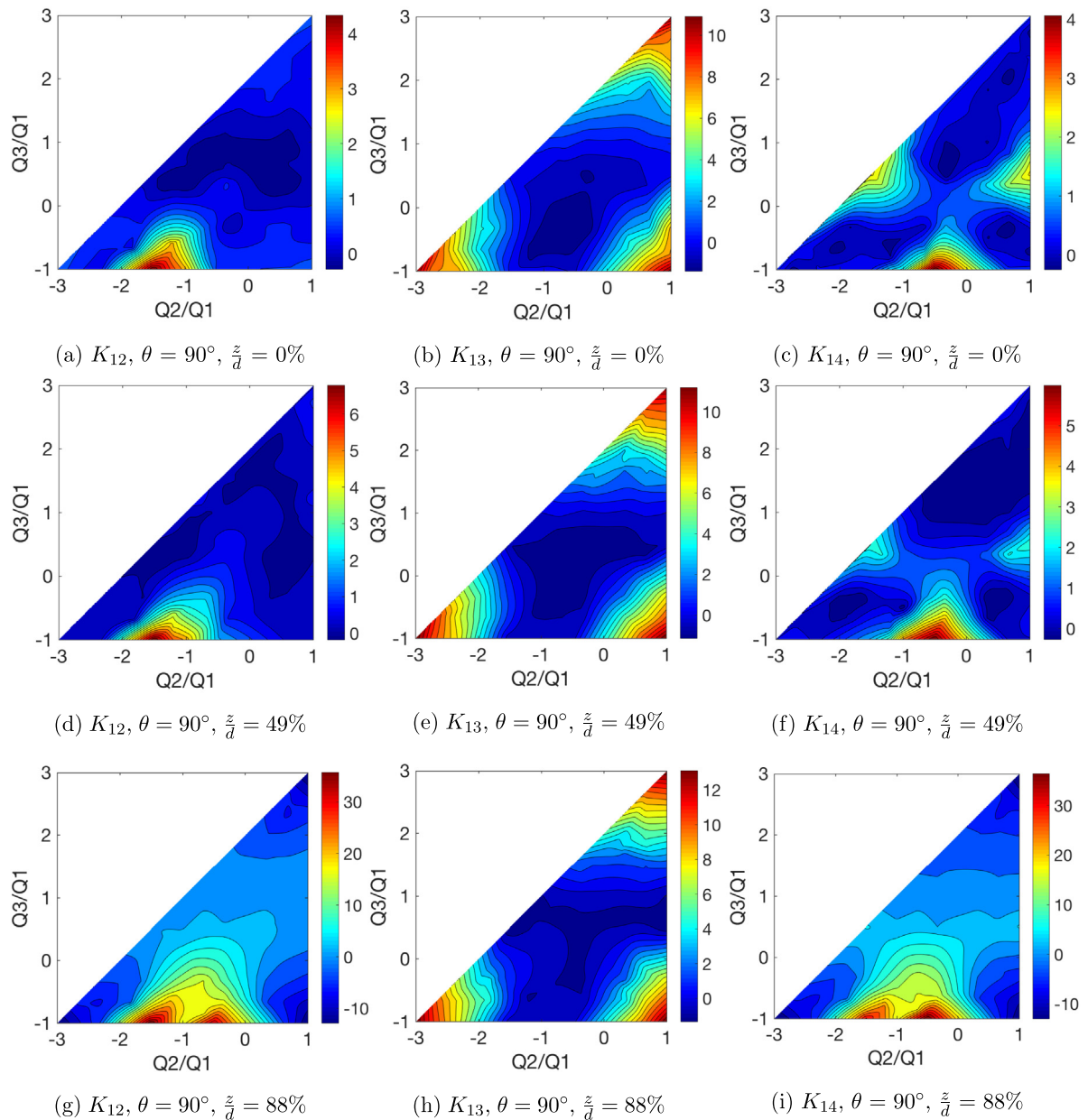


Fig. 11. Loss coefficients $\theta = 90^\circ$ orientation at full range of offsets.

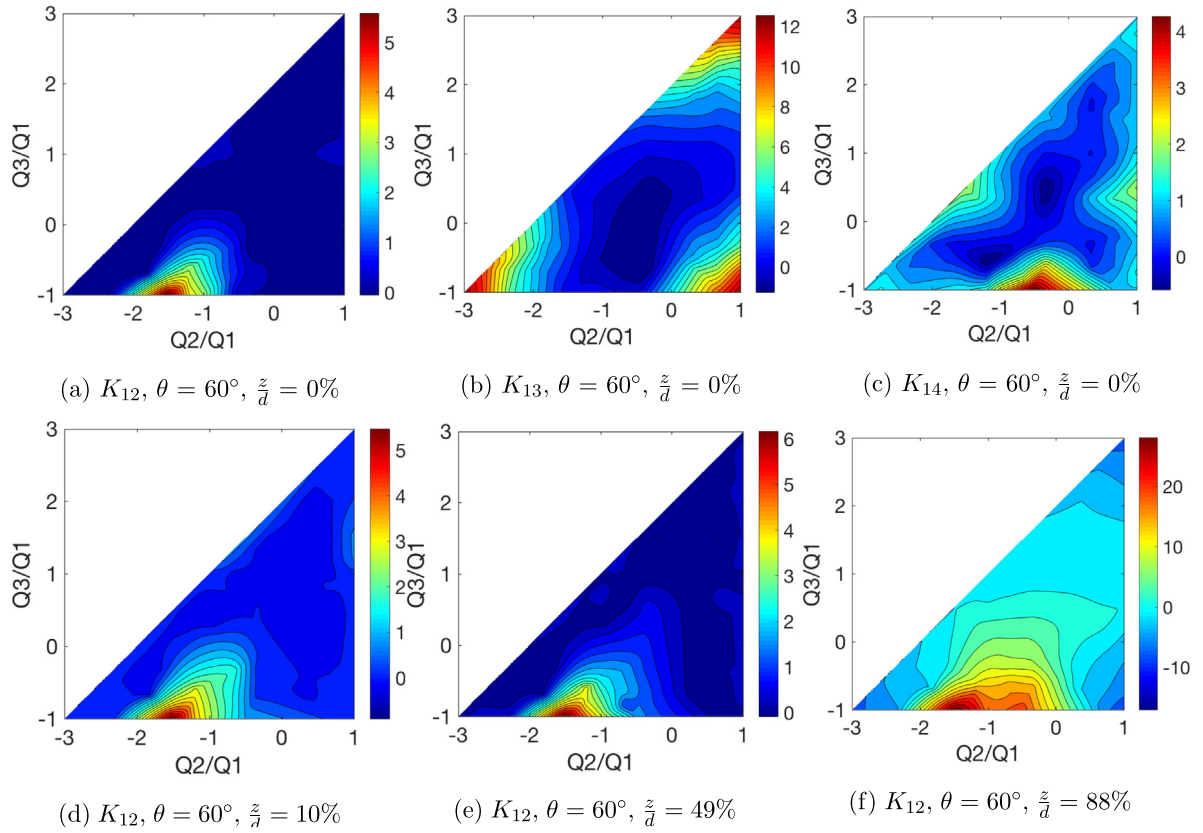
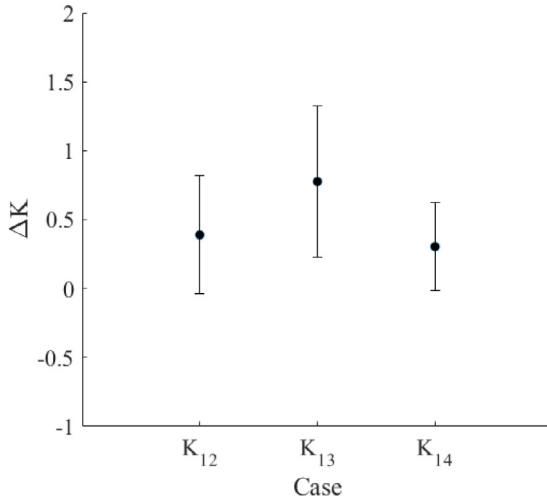
3 respectively, but as the offset increases there is initially mixing of flows and at the highest offset the flow from inlets 1 and 2 pass without turning largely to outlets 3 and 4 respectively. This results in almost no change in loss between the inlets (K_{12}), but for inlet to orthogonal outlet, the turning loss K_{14} is reduced as the flow entering from inlet 1 is reduced. Similarly, the loss to the co-aligned outlet K_{13} has a peak associated with inlet flow mixing at 10% offset, which reduces as the flow becomes more co-planar. In practice where the matrix is developed by drilling holes, of typical diameter 0.6 mm, a 50% error in $\frac{z}{d}$ is equivalent to a 0.3 mm misalignment which should be achievable for the laser or EDM machining of parts — even in a thick walled heat exchanger.

4.4. Heat transfer results

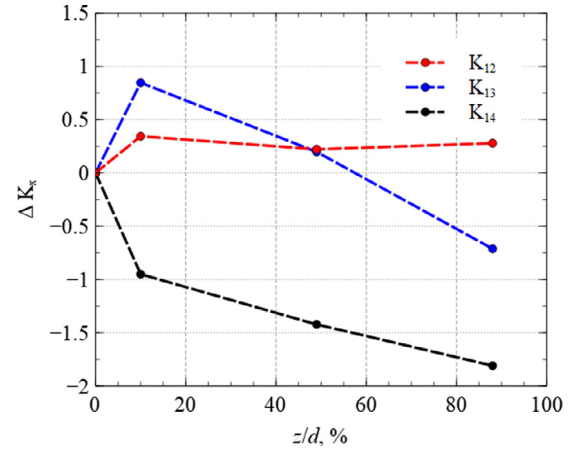
A primary aim of a cooling system, of course, is to remove heat from the blade. The internal cooling performance of intersecting systems is almost entirely unreported, therefore, here HTC distributions across

each intersection were obtained using the transient liquid crystal technique at a limited range of mass flow rates. A single heated incoming flow was used to determine the source of the heat transfer driving temperature.

HTC distributions are compared to CFD results for four cases representing a data point each from scenarios A,B,C and D. The agreement between the experimental and computational study was found to be excellent, accurately capturing regions with enhanced heat transfer within the experimental uncertainty bounds of the tests. Considering Fig. 17a, the region of high HTC downstream of the intersection can be attributed to several factors: First of all, the heated flow is being turned through 90° , with little or no heated flow from pipe 1 leaking into pipe 3. Hence the flow is impinging upon the surfaces in the downstream section and creating areas of higher heat transfer. By inducing turbulence in the downstream flow; the shear stresses in the flow increase, which introduces a higher bulk velocity gradient and increased heat transfer. Similar observations can be made regarding the other cases.

Fig. 12. Loss coefficients $\theta = 60^\circ$ orientation at $\frac{z}{d} = 0\%$.Fig. 13. Comparison between CFD and experimental results – 90° angle of intersection, 0% offset.

The system may be categorised as a three or four temperature problem depending on the number of inlets, but in actuality the density of intersection packing in a typical application and single upstream source of coolant means that it is sensible to regard the coolant as losing enthalpy at a uniform rate moving axially through the system, and thus the circumferentially averaged HTC distributions shown below are based on a single gas inlet temperature. The data, now all determined from CFD are normalised by the Dittus–Boelter turbulent pipe flow correlation, corrected for entry length effects (assuming a sharp-edged

Fig. 14. $Re_1 = 30,000$, $Re_2 = 30,000$, $Re_3 = 30,000$, $Re_4 = 30,000$.

inlet at the upstream edge of the domain).

$$HTC_{\text{normal}} = \frac{HTC_{\text{circumferentially averaged}}}{HTC_{\text{reference}}} \quad (9)$$

The results (which may also be considered Nusselt number enhancement) are shown in Fig. 18 for the four cases at all levels of offset. The Reynolds number used for normalisation across the full pipe was the inlet Reynolds number. In all cases the intersection is located at $L = 0.3$ m, and flow is in pipe 1 and pipe 3. It is at, or downstream of, the intersection that an immediate enhancement of heat transfer coefficient is seen. There is a clear relationship between changes in offset and maximum HTC for each scenario.

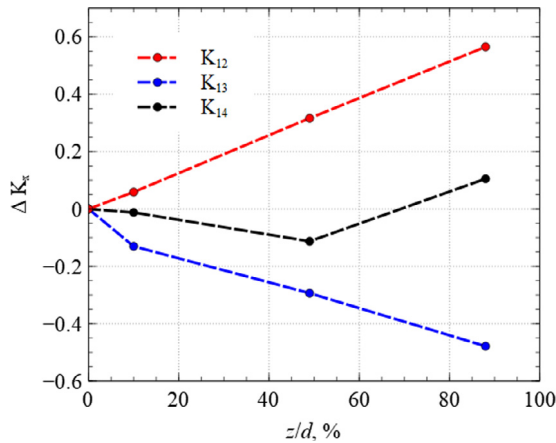


Fig. 15. $Re_1 = 30,000$, $Re_2 = 10,000$, $Re_3 = 30,000$, $Re_4 = 10,000$.

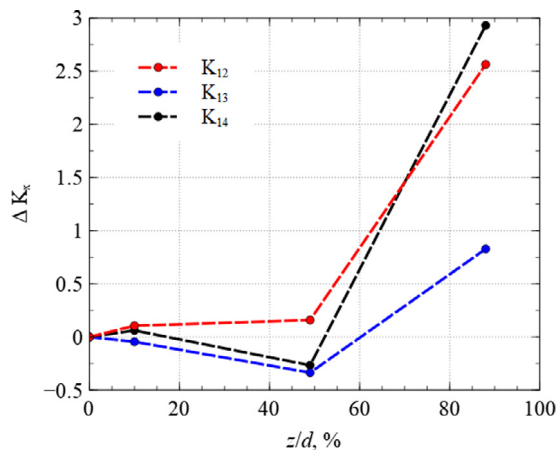


Fig. 16. $Re_1 = 30,000$, $Re_2 = 10,000$, $Re_3 = 10,000$, $Re_4 = 30,000$.

For Case A, a greater offset leads to lower heat transfer enhancement in pipe 3, as flow which impinges onto the wall of pipe 3 from pipe 2 is gradually replaced with through-flow from pipe 1. Thus an enhancement of 1.8 diminishes, essentially to the background level where $\frac{z}{d} = 88\%$. Note that it is quite legitimate for the enhancement to lie slightly below unity in these plots as the initial HTC values were based on the inlet driving gas temperature. The converse is true for Case B where the presence of three inlets results in higher HTC for a greater offset. Here the inlet flows from pipes 2 and 4 need to enter and, mix with the flow from pipe one then exit through pipe 3. The smaller the cross-over hole area, the faster the flow and more extreme the impingement on the opposite wall of the pipe. Thus the highest offset is associated with the highest HTC_{normal} of over 5. Case C displays two inlets from pipe 1 and 3. Here, again the highest rise in HTC_{normal} occurs for the 88% offset case and has a peak value of 1.6: the two inlet flows presented, which impinge before leaving the channel viewed here have a higher residence time in the passage when the exit hole is small, and the spatially larger extent of the enhancement is clear in the circumferentially averaged results. Finally, Case D shows little variation in the maximum HTC_{normal} between different offsets, with a slightly elevated maximum for the 10% offset. This case requires three outlets so similar levels of mixing is expected regardless of the offset. There is enhancement at the intersection through the renewal of the boundary layer but there is also a drop in HTC_{normal} after the intersection as the flow in this pipe is one third of the original value.

Table 3

The loss coefficient for each leg given spacing x/d .

Configuration	x/d	$K_{13,1st}$	$K_{24,1st}$	$K_{13,2nd}$	$K_{24,2nd}$
P	0	1.37	1.37	–	–
Q	10	1.39	1.41	1.49	1.41
R	20	1.40	1.39	1.38	1.40

5. Multiple intersections

The assumption that the pressure loss at single intersection can be used to predict loss in a matrix was examined for two coupled intersections using CFD for an extension of Case A. Here, there is equal mass flow in all pipes, two inlets at each intersection, 90° intersection and 0% offset. Spacing between intersections of 10 hole diameters is considered, which is typical of engine conditions. Fig. 19 shows the geometry employed for the additional branches with the spacings between intersections being $10d$ (Q) and a further case where the spacing is increased to $20d$ (R). These are compared to the single intersection case (P).

The loss coefficients K_{13} , and K_{24} were calculated, and values at the first and second intersection are shown for all configurations in Table 3. As expected, between the baseline (P) and Q there is no significant change in K_{13} (This is the loss between one inlet and an exit through which almost none of its flow passes). The increase of 0.1 in the $10d$ case between the $K_{13,first}$ and $K_{13,second}$ is driven by the non-uniform velocity field in the inlet to the second intersection which increases its average dynamic head compared to that based on the average velocity. The increase in $K_{13,first}$ in the $20d$ case is attributable to very small changes in the mass flow rate at convergence in the CFD study, and is insignificant. More interestingly $K_{13,first}$ and $K_{13,second}$ have very similar levels in this case (R) showing that the flow is more mixed out at the second intersection, eliminating the increase in K_{13} seen in the $10d$ case. In all cases the change in K_{13} is significantly less than that attributed above to changes caused by variation in offset.

The bulk observations are justified by the local pressure drop through the intersections: this was observed to be very close to equal at each intersection, and consistent with the results for a single intersection. Fig. 20 shows the pressure drop for the first and second intersections for each case. As expected, for the first intersection, the pressure drop for the single intersection is equal to the multiple case. With two intersections, when the distance between legs is short (Q), there is a larger pressure drop in the second leg than the first-driven by higher maximum velocities at the entry to branch 1 of the second intersection. However, as the distance increases, then it tends towards the pressure drop for a single intersection. This means that as long as enough section of pipe is maintained between intersections; each individual intersection can be treated individually (and hence the individual loss coefficient) for a multiple intersection system. It is noted that the maximum variation of 0.1 in K_{13} is 1% of its range for the 90° intersection case.

Fig. 21 shows that the HTC drops very slightly at the second intersection compared to the first. The higher upstream enhancement in HTC is consistent with a developing boundary layer, and the 5% reduction in the peak seen in the second intersection is associated with a reduction in the driving temperature potential in leg 1 of the second intersection. However, the intersection is clearly very effective in re-energising the downstream boundary layer at all intersections.

For a typical through flow energy balance solver used in the design of a blade or compact heat exchanger design, this changing driving temperature will be taken into account. The consistency of the HTC in both legs again suggests that it is possible to treat both legs as completely independent thus demonstrating the applicability of the data for more complex matrix analyses.

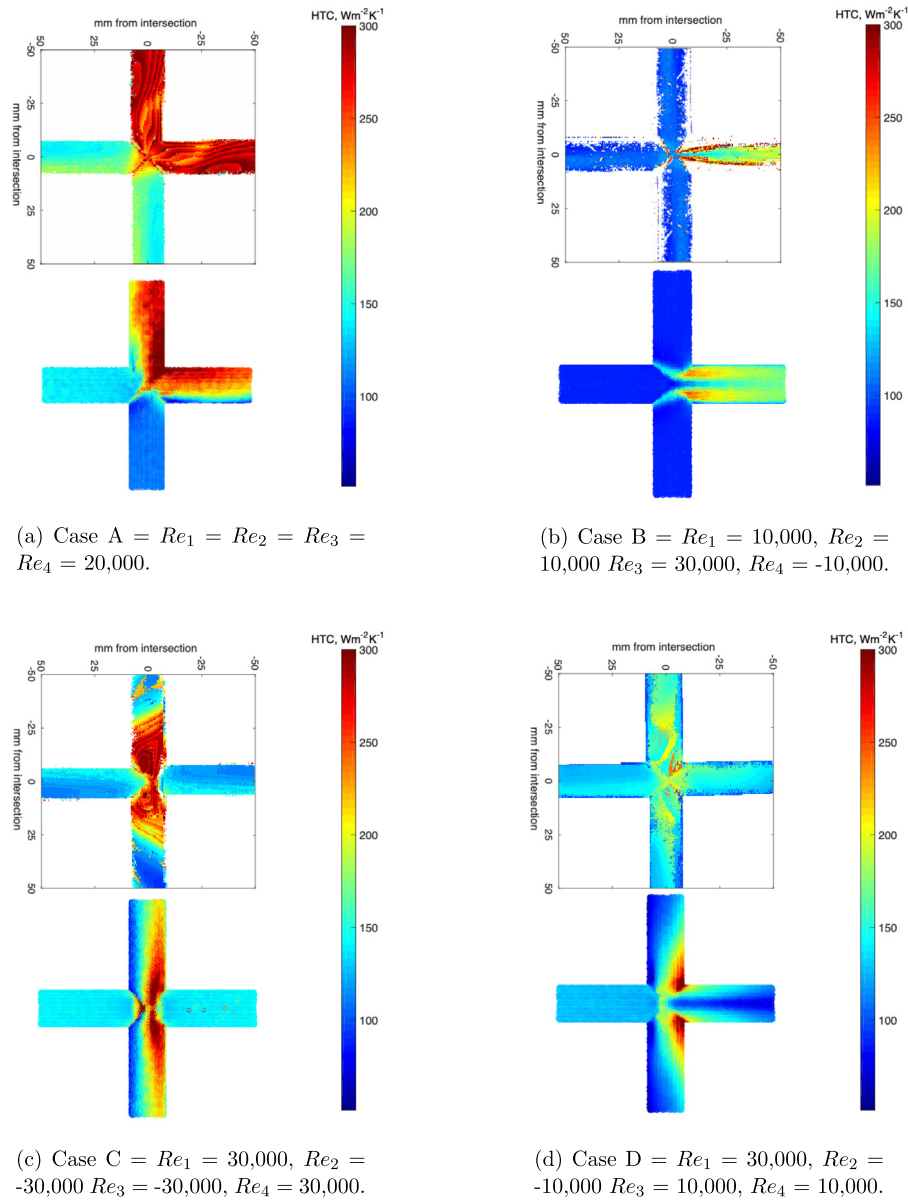


Fig. 17. Comparison of the HTC from CFD and TLC experiments, 90° angle of intersection, 0% offset, $d = 15.4$ mm, $T_{\text{gas}} = 70$ °C.

6. Conclusions

This paper has significantly extended previous work to improve understanding of the flow characteristics produced by intersecting cooling holes. An experimental campaign characterised single intersection losses for 90° and 60° intersections at $\frac{z}{d} = 0 - 88\%$. The results have shown large variations of losses for a given intersection geometry; with the losses strongly dependent on the mass flow splits at the inlet and outlet, but only weakly dependent on offset in the range 0%–49%.

In addition, the HTC distribution has been explored for several key intersection geometries with CFD studies seen to be in very good agreement with experimentally determined values. Nusselt number enhancement is associated with the renewal of the thermal boundary layer, mixing of the flow and impingement of the flow onto the pipe walls downstream of the intersections. Nusselt number enhancement levels of up to 5 were seen compared to fully developed turbulent flow, with regions of enhancement typically occurring over a distance of 1–1.5 d downstream of the intersection, and little enhancement occurring upstream.

Finally, the data for the individual intersections have been validated against multiple intersections. This provides a means to generate a full network flow and heat transfer analysis for a cooling matrix for use in the leading edge of a gas turbine blade, and provide a quick means for the optimisation of intersection packing such that a uniform external blade temperature can be achieved.

Declaration of competing interest

The authors declare that they have no known competing financial interests or personal relationships that could have appeared to influence the work reported in this paper.

Acknowledgements

The authors would like to extend their gratitude to Dr. Brian Tang for his help with using the THTAC software, Dr. Priyanka Dhopade for help post-processing the heat transfer data and Gerald for his care and attention manufacturing the perspex test pieces. The authors would also like to extend their gratitude toward the reviewers who improved the quality of this Paper.

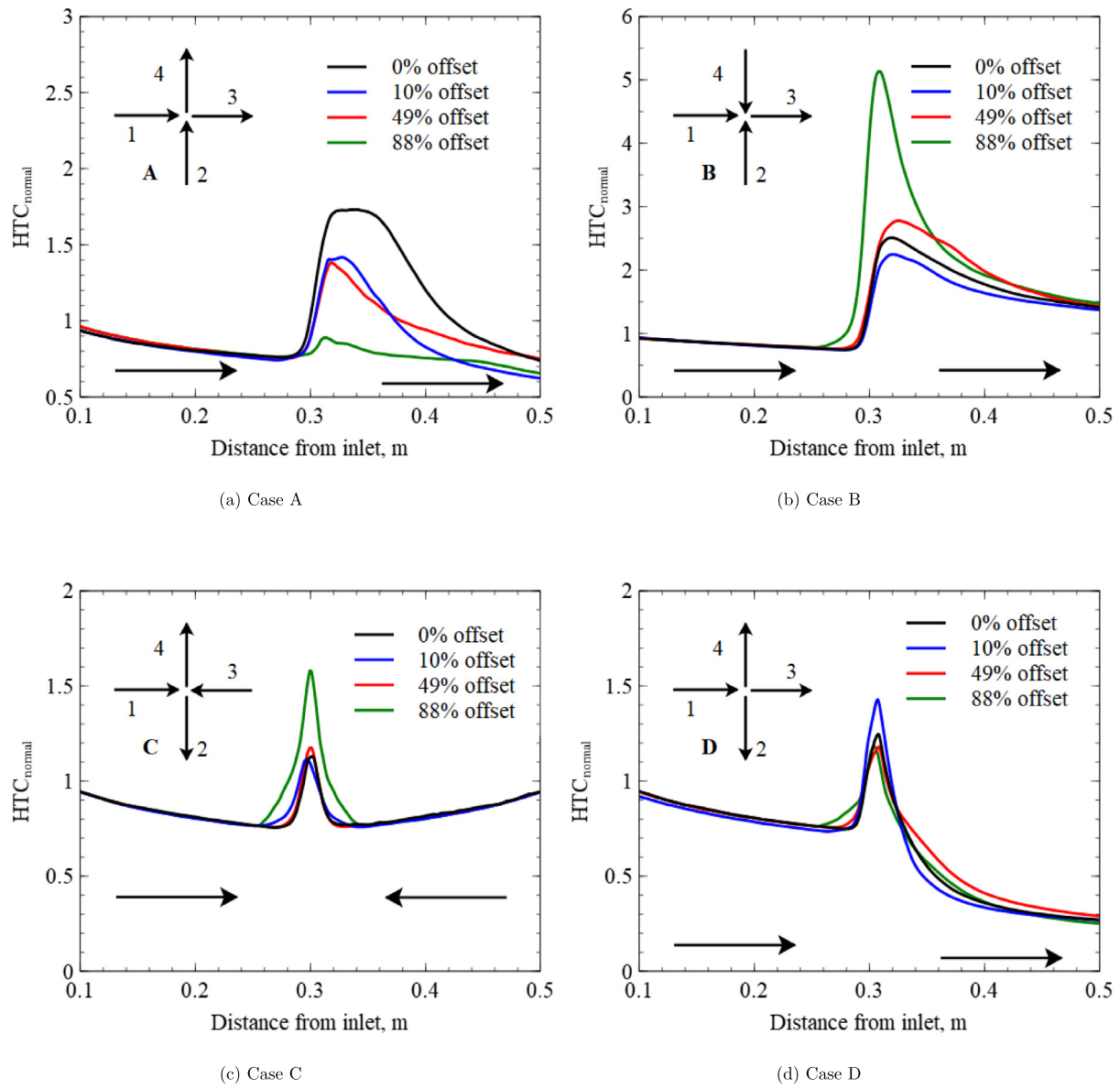


Fig. 18. Circumferentially averaged HTC along the cross-section from the beginning of pipe 1 to the end of pipe 3 ($\theta = 90^\circ$).

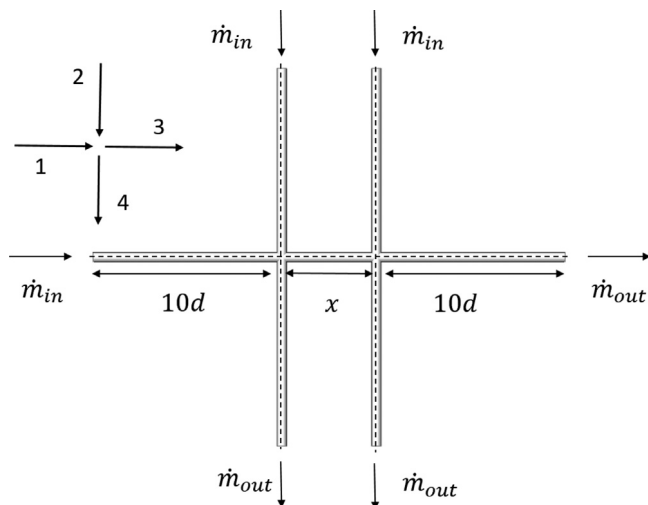


Fig. 19. Layout for the multiple intersection study.

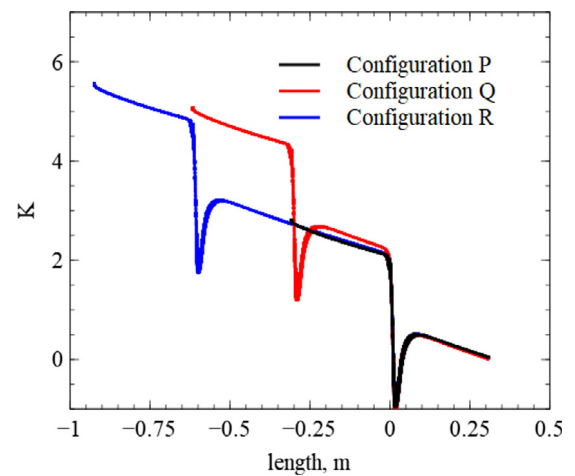


Fig. 20. Pressure drop across different multiple intersection configurations (from pipe 1 to 3).

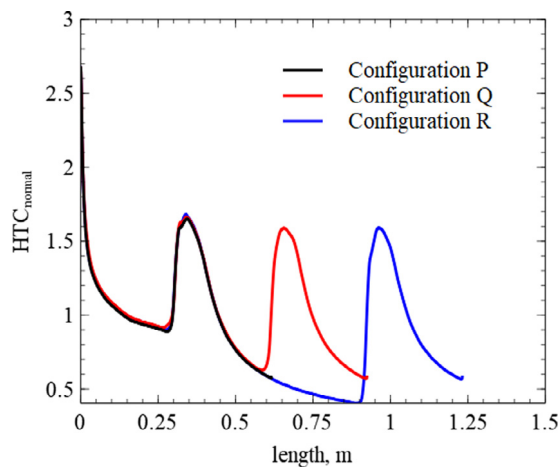


Fig. 21. HTC across different multiple intersection configurations (from pipe 1 to 3).

References

- [1] Y.I. Shanin, V.A. Afanas'ev, O.I. Shanin, Hydrodynamics and heat exchange in cooling systems with intersecting channels. I. Hydrodynamic characteristics, *J. Eng. Phys.* 61 (5) (1991) 1317–1324, <http://dx.doi.org/10.1007/BF00872247>.
- [2] N. Zhang, W.J. Yang, Y. Xu, C.P. Lee, Flow characteristics in flow networks, *Exp. Fluids: Exp. Methods Appl. Fluid Flow* 14 (1) (1993) 25–32, <http://dx.doi.org/10.1007/BF00196984>.
- [3] S.R. Nowlin, D.R.H. Gillespie, P.T. Ireland, R. Knoche, T.R. Kingston, A transient calorimeter technique for determining regional heat transfer coefficients in the three-temperature flowfield at a turbine airfoil leading edge, 2005, pp. 729–738, URL <http://dx.doi.org/10.1115/GT2005-68862>.
- [4] S.R. Nowlin, D.R.H. Gillespie, P.T. Ireland, E. Romero, M. Mitchell, An experimental and computational parametric investigation of flow conditions in intersecting circular passages, 2007, pp. 849–859, URL <http://dx.doi.org/10.1115/GT2007-28127>.
- [5] P.T. Ireland, T.V. Jones, Detailed measurements of heat transfer on and around a pedestal in fully developed passage flow, in: *Heat Transfer, Proceedings of the International Heat Transfer Conference, Vol. 3, 1986*, pp. 975–980.
- [6] P.M. Gerhart, R.J. Gross, J.I. Hochstein, *Fundamentals of Fluid Mechanics*, Addison-Wesley, 1992, URL <https://books.google.co.uk/books?id=r2EbAQAAIAAJ>.
- [7] Rolls-Royce, *The Jet Engine*, Wiley, 2005, URL <https://books.google.co.uk/books?id=kFElogEACAAJ>.
- [8] A.D. Fitt, C.J.P. Forth, B.A. Robertson, T.V. Jones, Temperature ratio effects in compressible turbulent boundary layers, *Int. J. Heat Mass Transfer* 29 (1) (1986) 159–164, [http://dx.doi.org/10.1016/0017-9310\(86\)90045-1](http://dx.doi.org/10.1016/0017-9310(86)90045-1), URL <http://www.sciencedirect.com/science/article/pii/0017931086900451>.
- [9] BS1042, *Measurement of Fluid Flow in Closed Conduits, I.1.1: Pressure Differential Devices*, British Standards Institution (BSI), 1989, URL <https://standards.globalspec.com/std/421525/BS%201042-1.2>.
- [10] J.R. Ryley, M. McGilvray, D. Gillespie, Local heat transfer coefficient measurements on an engine-representative internal cooling passage, *J. Thermophys. Heat Transfer* 33 (1) (2018) 189–198, <http://dx.doi.org/10.2514/1.T5206>.
- [11] R.J. Moffat, Contributions to the theory of single-sample uncertainty analysis, *J. Fluids Eng.* 104 (2) (1982) 250–258, URL <http://dx.doi.org/10.1115/1.3241818>.
- [12] J.P.C.W. Ling, P.T. Ireland, L. Turner, A technique for processing transient heat transfer, liquid crystal experiments in the presence of lateral conduction, *J. Turbomach.* 126 (2) (2004) 247, <http://dx.doi.org/10.1115/1.1740777>.